สัญญาเลขที่ R2558C113

รายงานวิจัยฉบับสมบูรณ์

การสร้างสัญญาณ WGM ระดับเท่าเฮิร์ตด้วย Micro-Conjugate Mirror เพื่อการตรวจติดตามและการประมวลผลสญัญาณเซลลส์มองในรูปแบบ 3 มิติ

ผู้ช่วยศาสตราจารย์ ดร.เกรียงศักดิ์ เตมีย์
ภาควิชาวิทยาการคอมพิวเตอร์และเทคโนโลยีสารสนเทศ
คณะวิทยาศาสตร์ มหาวิทยาลัยนเรศวร

สนับสนุนโดยกองทุนอุดหนุนวิจัยมหาวิทยาลัยนเรศวร

กิตติกรรมประกาศ

โครงการวิจัยนี้ได้รับทุนอุดหนุนจากงบประมาณรายได้ ทุนอุดหนุนการวิจัย มหาวิทยาลัยนเรศวร ประจำปีงบประมาณ พ.ศ. 2557 วงเงินงบประมาณ 180,000 บาท

ขอขอบคุณภาควิชาวิทยาการคอมพิวเตอร์และเทคโนโลยีสารสนเทศ คณะวิทยาศาสตร์ มหาวิทยาลัยนเรศวร ที่ให้การสนับสนุนวัสดุอุปกรณ์ รวมถึงสถานที่ในการทำวิจัย

ประโยชน์อันพึงมีจากรายงานวิจัยฉบับนี้ ผู้จัดทำขอมอบให้กับผู้มีพระคุณทุกท่าน หากรายงานฉบับนี้มีข้อผิดพลาดประการใดผู้จัดทำขอน้อมรับไว้เพียงผู้เดียว

เกรียงศักดิ์ เตมีย์

Abstract

In this research, a brain signal monitoring system using micro-optical conjugate mirror based on whispering gallery modes (WGMs) of light within a PANDA ring circuit is modeled and proposed. WGMs are generated by the PANDA ring circuit, which can be used to perform the brain signal connection using WGM probe, which is a 3D light probe. Simulation results obtained have shown that the THz WGMs can be generated and used as a probe to penetrate and connect to the brain cells and signals, which can be useful for brain signal monitoring and investigation. In applications, the various features such as smart multimedia devices, disability assisted and rehabilitation system, brain signal monitoring, robotic control and medical etc. using the THz 3D imaging probe can be plausible.

Contents

CHAPTER 1

INTRODUCTION

1.1 Introduction

Brain signals as a result of electrical activity that can be detected from the brain and also the primary sources for all communications by human perception, which is displayed in the form of brainwaves. They are very important to keep them with top security and fast link to the required destinations, for instance human organs and external link. Brain signals have been the important issue of research and investigations because they are the primary sources that can be used to perform all human communications [1]. One of the challenges and interesting is the use of brain signals to control various functions by the brain control system, which is known as brain computer interface (BCI), in which the developments of brain signals and related activities for various fields including cognitive neuroscience, medical, cognitive science, computer science, and psychology etc. are the important targets [2]. In addition, the new advances in computer technology and medical care have been expanded and become an integration of following technologies such as artificial intelligence, simulation, systems engineering and management knowledge [3]. These insights have been integrated to develop the ways to overcome health problems and become a modern medicine, where the use such as computer-assisted surgery (CAS) approach for optical intra-operative 3D reconstruction in laparoscopic surgery [4], computer-mediated medical information [5] has been reported.

New technologies that should be studied and developed for use with brain signal can be formed by various models, which require a high level of security. The application of specific properties of terahertz technology will be satisfied and discussed in the next paragraphs. Terahertz technology has become a tool that is very interesting in order to model and contribute the 3D image investigations, where the use such as the fabrication and testing of terahertz computer-generated volume holograms [6], terahertz imaging system [7] based on a quantum cascade laser (QCL) have been reported. THz has a frequency range from 0.3 THz to 10 THz in the electromagnetic spectrum, which is the range of frequencies that they are invisible to naked eye. One of the interesting features is the benefit of using terahertz waves that can penetrate through clothing, paper, or even into

human tissue, which can be very useful for medical sensing applications [8] and especially, when they are combined with the knowledge in biomedical researches [9-12], which have shown the results with higher promising applications, including brain, breast, skin, and hard tissue imaging / spectroscopy researches and investigations [13]. In addition, terahertz technology has been improved and continued development with techniques for testing and proof in order to obtain the results with 3D image presentation, for instance, the THz 3D imaging strategy using synthetic aperture radar (SAR) technique [14]. Till date, the new technique of 3D image presentation is still the challenge. Recently, WGM generated by optical resonators have demonstrated the interesting results, which have been the focus of an increasing amount of scientific researches in recent years [15]. Since 1991, InGaAsP/InP thin circular disks by chemical etching, which was demonstrated that the WGM lasing action at wavelength of 1.3 and 1.5 μm could be achieved [16]. After that the WGM has presented that the low cost and sensitive sensor [17] can be obtained and very useful to detect and distinguish between two biological such as DNA segments with slight difference in dielectric properties. The use of WGMs has been more successful after the announcement of Nobel Prize 2012 in Physics on the WGMs, where Yupapin et al have confirmed that WGMs can be generated due to coupling effects of the two nonlinear side rings of wave in PANDA ring [18]. In application, the PANDA ring can be experienced to be many devices such as the accuracy and precision on small scale optical devices of the applied sensors, which has shown the potential of using for such requirements [19, 20], the wave particle duality (WPD) probe using THz light pulse propagation within a micro-optical device system for consciousness and sub-consciousness [21], where the model of space-time paradox concept is useful for possible mind and dream investigations [22]. Moreover, the nested nonlinear micro-ring resonators (NMRs) and gratings can be useful for Cerenkov radiation investigation, imaging, and sensing applications [23], which is useful for consciousness and sub-consciousness investigations under the Cerenkov radiation.

In this report, we have proposed the small scale optical device system that can be processed with the principles of signal processing and monitoring brain signals in the form of a signal into a 3D image. By using the advantage of THz WGM signals, which can be formed by using the PANDA ring circuit, in which the brain signals can be probed and connected to the electronic instruments. Moreover, the brain signal can also be formed by the 3D image by using the conjugate mirror construction, which can be useful for many applications such as computer, multimedia devices, robotic control and medical etc.

CHAPTER 2

THEORETICAL BACKGROUND

2.1 Ring Resonators

A ring resonator is simply a waveguide shaped into a ring structure as shown in Fig. 2.1. When an input electric field, E_i, is coupled to the ring waveguide through an external bus waveguide, a positive feedback is induced and the field inside the ring resonator E_r, starts to build up. Coupling between the straight and the ring waveguide is achieved through the evanescent wave. Therefore, the gap and coupling length between them determine how much power is coupled from the straight waveguide to the ring waveguide and vise versa. In such configuration, only certain wavelengths will be allowed to resonate inside the ring waveguide, thus frequency selectivity is obtained. A resonant mode will have a wavelength that satisfies.

$$m\lambda_m = nL, \quad \text{m = integer} \tag{2.1}$$

Here, m is the longitudinal mode number, λ_m is the resonant mode wavelength, n is the refractive index of the guiding material, and L is the circumference of the ring resonator.

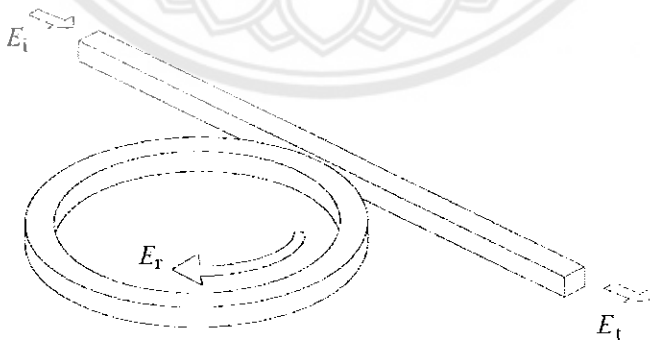

Fig. 2.1 Schematic diagram for a ring resonator coupled to a single waveguide.

A ring resonator device is promising candidates for wavelength filtering, multiplexing/demultiplexing, conversion and network routing application. Two typical settings of ring resonator are shown in Fig. 2.2. A ring or a disk shaped dielectric cavity is

placed between two parallel dielectric straight waveguides. In real life (3-D) devices, the straight waveguides can be positioned either in the same plane (Fig. 2.2(a): horizontal coupling scheme) or below (Fig. 2.2(b): vertical coupling scheme) the cavity plane. These two straight waveguides form four ports for the external connections, the two input ports named "In-port" And "Add-port", and the two output ports named "Through-port" and "Drop-port". To understand the functioning of the ring resonator, for the sake of simplicity, let's consider only unidirectional fields (clockwise propagating), where only the In-port is illuminated, while there is no incoming signal at the Add-port.

Conventionally, the functioning of ring resonator is described by the interaction of harmonic optical waves propagating along the straight waveguide and the cavity, and the interferometric resonances of the waves inside the cavity. A single frequency optical wave is launched at the In port of the resonator. As this signal propagates along the upper straight waveguide, that connects the In-port and Through-port, part of it is evanescently coupled to the cavity. While propagating along the cavity, part of this signal is coupled to the lower straight waveguide and appears at the Drop-port. The remaining part of the signal propagates along the cavity, and interferes with the newly in-coupled signal in the upper interaction region. Depending upon the specific configuration, these two fields undergo constructive or destructive interference.

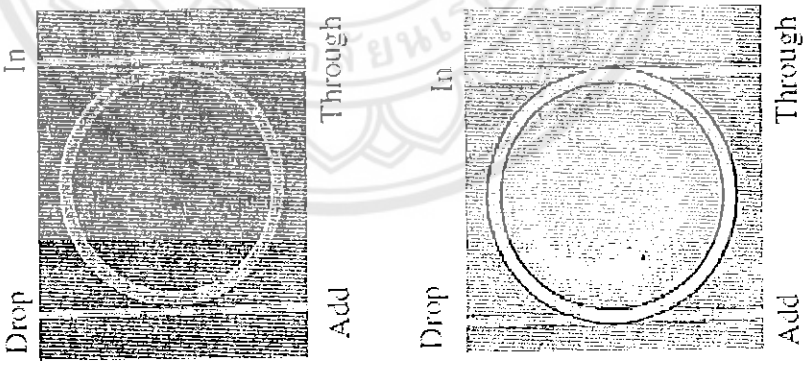

(a) (b)

Fig. 2.2 Scanning electron microscope pictures of horizontally coupled (a) and vertically coupled (b) real life ring resonator.

If the cavity field is out of phase with the newly entering field, then destructive interference takes place inside the cavity and as a result, there is only a small amount of power inside the cavity. Under so-called off resonance conditions, as shown in Fig. 2.3(a),

most of the input power is directly transmitted to the Through-port, and there is comparably low power at the Drop-port.

On the other hand, if the field inside the cavity is in phase with the newly in-coupled signal, then due to constructive interference, energy builds up inside the cavity. This field gets coupled to the Drop-port waveguide. Under so-called resonance conditions, there is a signi_cant power observed at the Drop-port, while less power appears at the Through-port. This situation is shown in Fig. 2.3(b).

A typical spectral response of a ring resonator device is shown in Fig. 2.3(c). Resonance appears as dips in the Through-port power curve and peaks in the Drop-port power curve. In other words, the wavelength for which ring resonator is on resonance, will be "dropped" at the Drop port. Also, for a symmetrical device, if a new signal that corresponds to a resonance wavelength is launched at the Add-port, it will get .added. to the off resonance signal launched at the input port, and appears at the throughput port. Therefore the arrangement shown in Fig. 2.2 can be used as an add/drop filter.

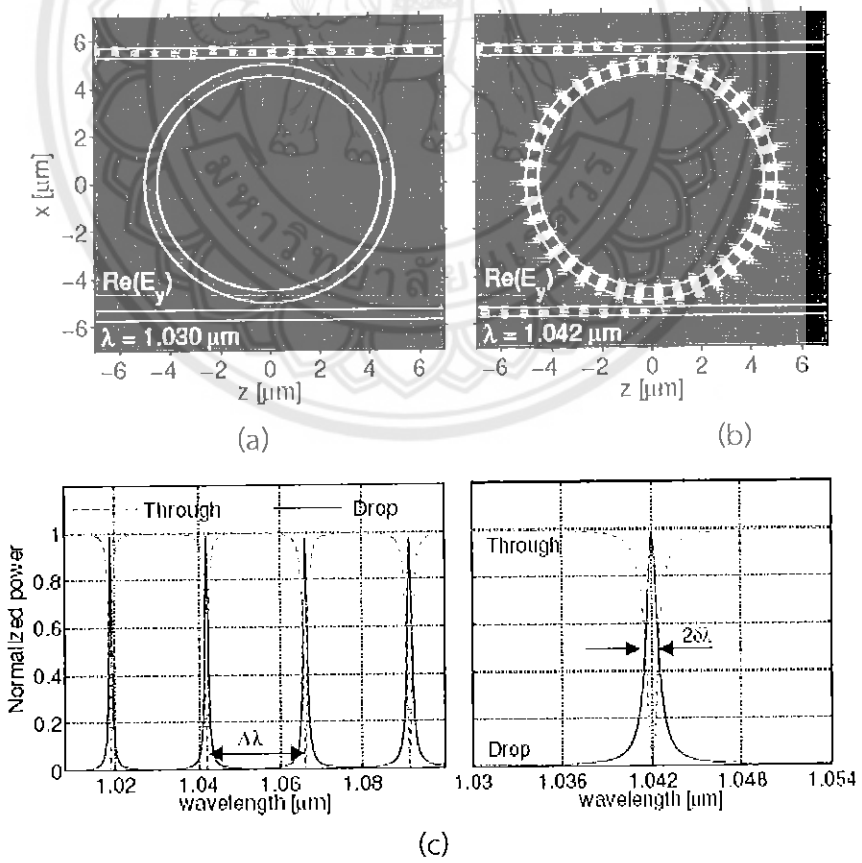

Fig. 2.3 Simulated response off-resonance state (a) and resonance state (b) of a ring resonator. Also shown is the wavelength dependent response of the ring resonator (c).

2.2 The ring resonator – the used model

A single ring resonator is transferred into a box like filter shape using a single coupler or a double

coupler configuration as shown in Figs 2.4 and 2.5. A calculation model is derived and all essential parameters describing the transmission characteristic are extracted in this section.

2.2.1 Single Coupler Ring Resonator Filter (SCRR)

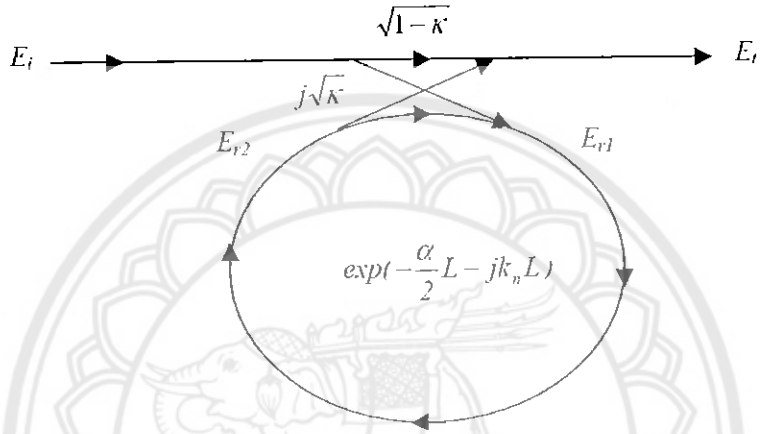

Fig. 2.4 Schematic diagram for a ring resonator coupled to a single waveguide

The transfer function of this configuration is derived using Z-transform analysis. The circumference of the ring is L ($L = 2\pi R$, the radius is R), the coupling coefficient of the coupler is κ. The Z-transform parameter is represented by $z^{-1} = \exp^{-jk_nL}$ where $k_n = \frac{2\pi}{\lambda} n_{eff}$ is the propagation constant and n_{eff} is the effective index of the waveguide. The one round trip loss is $a = \exp^{-\alpha L/2}$, α is the intensity attenuation coefficient inside the waveguide [unit $length^{-1}$]. The transmitted or throughput field at the output of the straight waveguide, E_t and inserted electric field, E_i relations can be derived as followed:

$$E_t = (1-\gamma)^{1/2} \times \left[E_i \cdot \sqrt{1-\kappa} + j \cdot E_{r2}\sqrt{\kappa}\right]. \tag{2.2}$$

$$E_{r1} = (1-\gamma)^{1/2} \times \left[j \cdot E_i \cdot \sqrt{\kappa} + E_{r2} \cdot \sqrt{1-\kappa}\right]. \tag{2.3}$$

$$E_{r2} = E_{r1} \cdot a\, z^{-1}. \tag{2.4}$$

Using these equations, E_t / E_i can be calculated:

$$\frac{E_t}{E_i} = (1-\gamma)^{1/2} \times \left[\frac{\sqrt{1-\kappa} - (1-\gamma)^{1/2} \cdot a\, z^{-1}}{1 - (1-\gamma)^{1/2} \cdot \sqrt{1-\kappa} \cdot a\, z^{-1}} \right]. \tag{2.5}$$

The transfer function in Eq. (2.5) indicates that a ring resonator is very similar to a Fabry-Perot cavity. In the particular case shown in Fig. 2.4, the corresponding Fabry-Perot cavity would have an input mirror with a field reflectivity and a fully reflecting output mirror. However, the field propagating inside the ring cavity is a traveling wave in contrast to the Fabry-Perot cavity which resonates a standing wave.

In the following, new parameter will be used for simplification:

$$\begin{aligned} D &= (1-\gamma)^{1/2} \\ x &= D \cdot \exp^{-\alpha L/2} \\ y &= \sqrt{1-\kappa} \\ \phi &= k_n \cdot L \end{aligned} \tag{2.6}$$

The intensity relation for the output port is given by:

$$T = \frac{I_t}{I_i}(\phi) = \left| \frac{E_t}{E_i} \right|^2 = D^2 \cdot \left[1 - \frac{(1-x^2)\cdot(1-y^2)}{(1-x\cdot y)^2 + 4\cdot x\cdot y\cdot sin^2\left(\frac{\phi}{2}\right)} \right]. \tag{2.7}$$

2.2.2 Double Coupler Ring Resonator Filter (DCRR)

Consider the architectures of double coupler ring resonator which sometime called add/drop filters as illustrated in Fig. 2.5, which are constructed by 2×2 optical couplers.

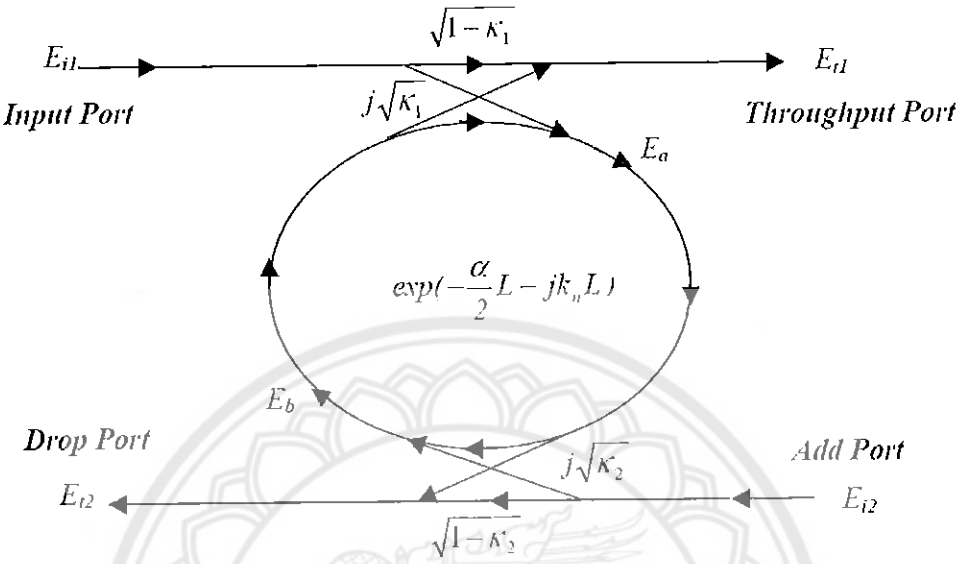

Fig. 2.5 The single ring resonator with two adjacent waveguides

For simplification, the calculation of the intensity relation does not take into account coupling losses ($D^2 = 1$).

$$E_a = E_{i1}\, j\sqrt{\kappa_1} + E_b\sqrt{1-\kappa_1}\, e^{-\frac{\alpha L}{2\,2} - jkn\frac{L}{2}} \tag{2.8}$$

$$E_b = E_a\sqrt{1-\kappa_2}\, e^{-\frac{\alpha L}{2\,2} - jkn\frac{L}{2}} \tag{2.9}$$

$$E_a = \frac{E_{i1}\, j\sqrt{\kappa_1}}{1-\sqrt{1-\kappa_1}\sqrt{1-\kappa_2}\, e^{-\frac{\alpha}{2}L - jknL}} \tag{2.10}$$

$$E_b = \frac{E_{i1}\, j\sqrt{\kappa_1}}{1-\sqrt{1-\kappa_1}\sqrt{1-\kappa_2}\, e^{-\frac{\alpha}{2}L - jknL}} \cdot \sqrt{1-\kappa_2}\, e^{-\frac{\alpha L}{2\,2} - jkn\frac{L}{2}} \tag{2.11}$$

$$E_{t1} = E_b\, j\sqrt{\kappa_1}\, e^{-\frac{\alpha L}{2\,2} - jkn\frac{L}{2}} + E_{i1}\sqrt{1-\kappa_1} \tag{2.12}$$

$$E_{t2} = E_a\, j\sqrt{\kappa_2}\; e^{-\frac{\alpha L}{2 2} - jkn\frac{L}{2}} \qquad at \;\; E_{i2} = 0 \tag{2.13}$$

Where E_{i1} is the input field, E_{t1} is the throughput field, E_{t2} is the dropped field, E_{t1}, E_a and E_b are the fields in the ring, κ_1 is thefield coupling coefficient between the input bus and the ring, κ_2 is the field coupling coefficient between the ring and the input bus, L is the circumference of the ring,

By using the upper equations, the transfer function for throughput port and drop port in Fig. 2.5 can thus be expressed as

Throughput port:

$$\frac{E_{t1}}{E_{i1}} = \frac{-\kappa_1\sqrt{1-\kappa_2}\; e^{-\frac{\alpha}{2}L - jknL} + \sqrt{1-\kappa_1} - (1-\kappa_1)\sqrt{1-\kappa_2}\; e^{-\frac{\alpha}{2}L - jknL}}{1 - \sqrt{1-\kappa_1}\sqrt{1-\kappa_2}\; e^{-\frac{\alpha}{2}L - jknL}} \tag{2.14}$$

$$\frac{E_{t1}}{E_{i1}} = \frac{-\sqrt{1-\kappa_2}\; e^{-\frac{\alpha}{2}L - jknL} + \sqrt{1-\kappa_1}}{1 - \sqrt{1-\kappa_1}\sqrt{1-\kappa_2}\; e^{-\frac{\alpha}{2}L - jknL}} \tag{2.15}$$

Drop port:

$$\frac{E_{t2}}{E_{i1}} = \frac{-\sqrt{\kappa_1\kappa_2}\; e^{-\frac{\alpha L}{2 2} - jkn\frac{L}{2}}}{1 - \sqrt{1-\kappa_1}\sqrt{1-\kappa_2}\; e^{-\frac{\alpha}{2}L - jknL}} \tag{2.16}$$

The intensity relations for the throughput and drop port can be obtained by normalizing the transfer functions in Eqs. (2.17) and (2.18) which are given by

$$\frac{I_{t1}}{I_{i1}} = \left|\frac{E_{t1}}{E_{i1}}\right|^2 = \frac{1-\kappa_1 - 2\sqrt{1-\kappa_1}\sqrt{1-\kappa_2}\; e^{-\frac{\alpha}{2}L}\cos(knL) + (1-\kappa_2)\, e^{-\alpha L}}{1 + (1-\kappa_1)(1-\kappa_2)e^{-\alpha L} - 2\sqrt{1-\kappa_1}\sqrt{1-\kappa_2}\; e^{-\frac{\alpha}{2}L}\cos(knL)} \tag{2.17}$$

$$\frac{I_{t2}}{I_{i1}} = \left|\frac{E_{t2}}{E_{i1}}\right|^2 = \frac{\kappa_1\kappa_2\, e^{-\frac{\alpha}{2}L}}{1 + (1-\kappa_1)(1-\kappa_2)e^{-\alpha L} - 2\sqrt{1-\kappa_1}\sqrt{1-\kappa_2}\; e^{-\frac{\alpha}{2}L}\cos(knL)} \tag{2.18}$$

2.3 PANDA ring resonator

A "PANDA" ring resonator is a modified add/drop optical filter that was proposed by Yupapin et al [23] that can be applied to many applications by changing the structure of PANDA and signal, as a suitable candidate for sensing device construction [19, 20].

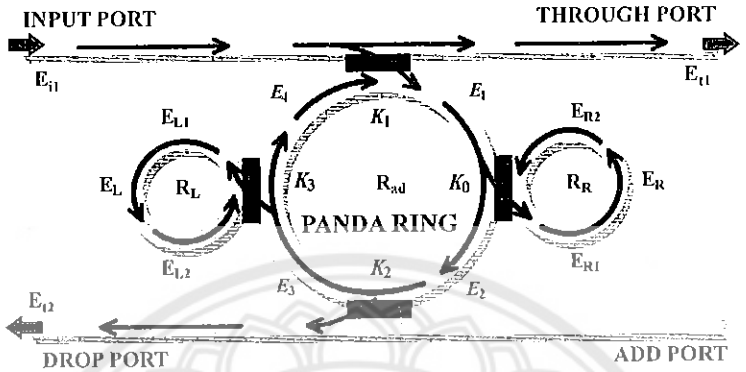

Fig. 2.6. A schematic diagram of a PANDA ring resonator system

The schematic diagram of a PANDA ring resonator system for transfer function is shown in Fig. 2.6, which the calculation of the intensity relation does not take into account coupling losses can be written as

$$E_1 = j\sqrt{K_1 x_1} \bullet E_{i1} + j\sqrt{K_1 x_1 y_1 y_2} \bullet E_{i2} \bullet E_L \bullet e^{-\frac{aL}{22} - jk_n \frac{L}{2}} \tag{2.19}$$

$$E_2 = E_r \bullet E_1 \bullet e^{-\frac{aL}{22} - jk_n \frac{L}{2}} \tag{2.20}$$

$$E_3 = jx_2 E_{i2} + x_2 y_2 E_r \bullet E_1 \bullet e^{-\frac{aL}{22} - jk_n \frac{L}{2}} \tag{2.21}$$

$$E_4 = j\sqrt{K_2 x_2} \bullet E_{0L} \bullet E_{i2} + x_2 y_2 E_r \bullet E_1 \bullet E_L \bullet e^{-\frac{aL}{22} - jk_n \frac{L}{2}} \tag{2.22}$$

where $x_1 = \sqrt{1-\gamma_1}, x_2 = \sqrt{1-\gamma_2}, y_1 = \sqrt{1-K_1}$, and $y_2 = \sqrt{1-K_2}$

$$E_{t1} = AE_{i1} - BE_{i2}e^{-\frac{\alpha L}{2}-jk_n\frac{L}{2}} - \left[\frac{CE_{i1}\left(e^{-\frac{\alpha L}{2}-jk_n\frac{L}{2}}\right)^2 + DE_{i2}\left(e^{-\frac{\alpha L}{2}-jk_n\frac{L}{2}}\right)^3}{1-F\left(e^{-\frac{\alpha L}{2}-jk_n\frac{L}{2}}\right)^2}\right], \quad (2.23)$$

where

$A = \sqrt{(1-K_1)(1-\gamma_2)}$,

$B = \sqrt{(1-\gamma_1)(1-\gamma_2)K_2(1-K_1)E_L}$,

$C = K_1(1-\gamma_1)\sqrt{(1-\gamma_2)K_2E_rE_L}$,

$D = (1-\gamma_1)(1-\gamma_2)\sqrt{(1-K_1)(1-K_2)E_rE_L^2}$, and

$E = (1-\gamma_1)(1-\gamma_2)\sqrt{(1-\gamma_1)(1-\gamma_2)(1-K_1)(1-K_2)E_rE_L}$,

where E_{t1} and E_{t2} are the optical fields of the through and drop ports respectively, $\beta = kn_{eff}$ is the propagation constant, n_{eff} is the effective refractive index of the waveguide, and the circumference of the ring is $L = 2\pi R$ where R is the radius of the ring. K_1 and K_2 are the coupling coefficients of the add/drop filters, $k_n = 2\pi/\lambda$ is the wave propagation number in a vacuum, and the waveguide (ring resonator) loss is $\alpha = 0.5dBmm^{-1}$. The fractional coupler intensity loss is $\gamma = 0.1$. In the case of the add/drop device, the nonlinear refractive index does not affect the system, and therefore it is neglected. The electric field E_r and E_L are the field circulated within the nano-ring at the right and left side of the add/drop optional filter. The power output (P_{t1}) at the through port is written as:

$$P_{t1} = |E_{t1}|^2 \quad (2.24)$$

The output field (E_{t2}) at the drop port is expressed as:

$$E_{t2} = \sqrt{(1-\gamma_2)(1-K_2)}E_{i2} - \left[\frac{\sqrt{(1-\gamma_2)(1-K_2)K_1K_2E_0E_{i1}}e^{-\frac{\alpha L}{2}-jk_n\frac{L}{2}} + XE_rE_L\left(e^{-\frac{\alpha L}{2}-jk_n\frac{L}{2}}\right)^2}{1-YE_rE_L\left(e^{-\frac{\alpha L}{2}-jk_n\frac{L}{2}}\right)^2}\right] \quad (2.25)$$

where

$$X = (1-\gamma_2)\sqrt{(1-\gamma_1)(1-K_1)K_2(1-K_2)},\ Y = \sqrt{(1-\gamma_1)(1-\gamma_2)(1-K_1)(1-K_2)}.$$

The power output (P_{t2}) at the drop port is: $P_{t2} = |E_{t2}|^2$

CHAPTER 3

PANDA RING RESONATOR SENSOR

3.1 Introduction

In the recent years, optical sensors have been implemented and widely used in various applications, for instance, in medicine, microbiology, communication, particle physics, automotive, environmental safety and defense. Particularly, the integrated nonlinear optical device using a microring resonator has been widely investigated in both theory and experiment. One of the interesting results is the use of a specific model of a ring resonator known as a PANDA ring resonator, which can be a good candidate for nanoscale sensing applications. The use of nanoscale measurement with more efficiency systems has been reported by several research groups. However, the searching system has been presented by Yupapin et al , in which the interesting results are the self-calibration sensor base on ring resonator. Recently, the use of a new form of a ring resonator called a PANDA ring resonator has shown the interesting aspect of applications [12, 13]. The authors have shown that such a proposed form of a ring resonator can establish the new concept of dark-bright soliton collision, whereas the use of random encoding, optical vortices (tweezers) and optical/quantum gate can be generated. In this chapter, we propose the other aspect of a PANDA ring resonator, in which the system of a nano-scale sensing transducer based on a PANDA ring resonator type is proposed. In practical the sensing ring should be free-standing. Usually, if force is applied to a free-standing structure, it is bent. Hence, the shapes of the sensing ring are deformed into an ellipse and then induce the ring circumference-shift ΔL. The sensing system is functioned by mean of the change of a ring radius due to a load cell or other physical parameters, where the change in optical path length of light is caused by the same way of an interferometer, while the other ring radius is remain constant(reference). The sensing and the reference signals are analyzed, simulated and compared. Simulation results obtained have shown that the system can be employed to be the nano-scale sensing transducer. However, the measurement limitation is occurred due to wavelength meter resolution, in which the measurement resolution of 1 nm is noted in this work. Lastly,

the distributed or multiplexed sensing application is also available using the nano-scale sensing transducer via the multi wavelength router, which is discussed in details.

3.2 Principle and Method

To form the simulation sensing performance, the microring material used is InGaAsP/InP, with the refractive index is n_0 = 3.34 [45-47]. The schematic diagram of a sensing transducer using a PANDA ring resonator is as shown in Fig.3.1. The system consisted of three microring resonators, where the first ring is position as a reference ring, with radius R_1 = 1.550 μm. The second ring R_2 is the sensing ring, the radius is varied by mean of the deformation of ring radius due to an applied force or load cell, and the third ring is used to form the interference signal between reference and sensing rings, with the radius R_3 = 3.10 μm. In operation, the change in sensing ring radius is caused the change in the shift in signals circulated in the interferometer ring (R_3), in which the interference signals are seen. The change in optical path length which is related to the change of the external parameters is measured.

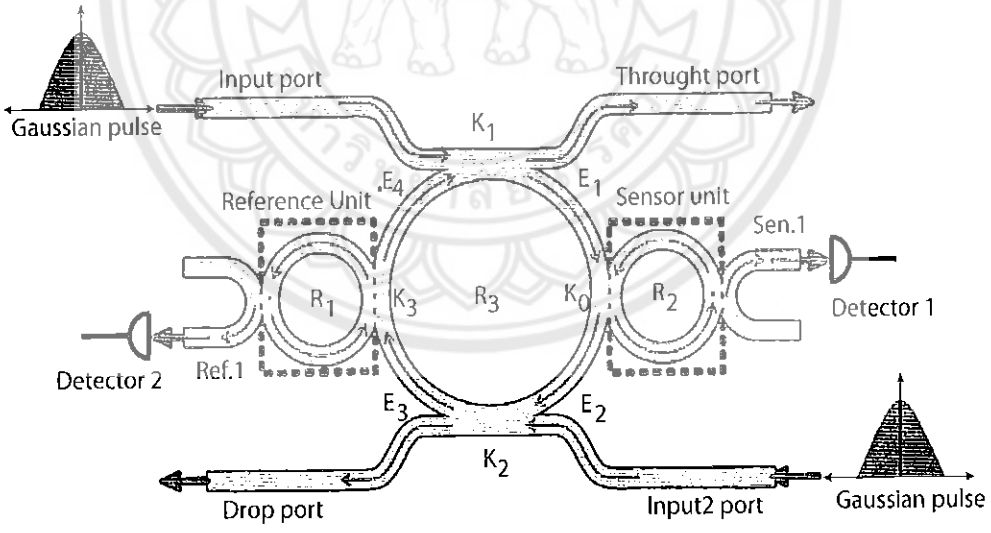

Fig.3.1. Schematic diagram of a nano-scale sensing transducer using a PANDA ring resonator.

Two identical beams of monochromatic optical field (E_{in}) of Gaussian pulse with the center wavelength 1.550 μm are launched into in the system at the input port and the add port, which is given by

$$E_{in}(t) = E_0 e^{[-\alpha L + j\phi_0(t)]} \tag{3.1}$$

where $L = 2\pi R$ is a propagation distance (waveguide length), α is an attenuation and ϕ_0 is the phase constant. When light propagates within the nonlinear material (medium), by using the Kerr nonlinear effect within the ring devices, the refractive index (n) of light within the medium is given by

$$n = n_0 + n_2 I = n_0 + n_2\left(\frac{P}{A_{eff}}\right) \tag{3.2}$$

where n_0 and n_2 are the linear and nonlinear refractive indices, respectively. I and P are the optical intensity and optical power, respectively. The effective mode core area of the device is given by A_{eff}.

The resonance output is formed, thus, the normalized output of the light field is the ratio between the output ant input fields $[E_{ih}(t) \text{ and } E_{in}(t)]$ in each roundtrip, which is given by [14, 37]

$$\left|\frac{E_{ih}(t)}{E_{in}(t)}\right|^2 = (1-\gamma)\left[1 - \frac{(1-(1-\gamma)x^2)\kappa}{\left(1-x\sqrt{1-\gamma}\sqrt{1-\kappa}\right)^2 + 4x\sqrt{1-\gamma}\sqrt{1-\kappa}\sin^2\left(\frac{\phi}{2}\right)}\right] \tag{3.3}$$

The optical output of ring resonator add/drop filter for the through and drop ports can be given by Eqs. (3.4) and (3.5), respectively [14]

$$\left|\frac{E_{t1}}{E_{in}}\right|^2 = \frac{(1-\kappa_1) - 2\sqrt{1-\kappa_1}.\sqrt{1-\kappa_2}.e^{\frac{-\alpha}{2}L}\cos(k_n L) + (1-\kappa_2)e^{-\alpha L}}{1 + (1-\kappa_1)(1-\kappa_2)e^{-\alpha L} - 2\sqrt{1-\kappa_1}.\sqrt{1-\kappa_2}e^{\frac{-\alpha}{2}L}\cos(k_n L)} \tag{3.4}$$

$$\left|\frac{E_{t2}}{E_{in}}\right|^2 = \frac{\kappa_1\kappa_2.e^{\frac{-\alpha}{2}L}}{1 + (1-\kappa_1)(1-\kappa_2)e^{-\alpha L} - 2\sqrt{1-\kappa_1}.\sqrt{1-\kappa_2}e^{\frac{-\alpha}{2}L}\cos(k_n L)} \tag{3.5}$$

Where E_{t1} and E_{t2} represent the optical fields of the through and drop ports, respectively. $x = \exp\left(-\alpha L/2\right)$ is a roundtrip loss coefficient, $k_n = 2\pi/\lambda$ is the wave propagation number in vacuum, n_{eff} is an effective refractive index, $\phi = kn_{eff}L$ is the phase constant, γ is the fractional coupler intensity loss, κ is the coupling coefficient, and β is a complex coefficient, The signals of both rings R_1 and R_2 are observed at the point Ref.1 (E_{R1}) and Sen.1 (E_{S1}) respectively as shown in Fig. 3.1, and the mathematical form of those signals are also analyzed, which can be expressed as

$$\left|\frac{E_{S1}}{E_{in}}\right|^2 = \left[\frac{-(1-\gamma_S)\kappa_S}{1-Z_2(1-\gamma_S)(1-\kappa_S)}\right]\left[\frac{j.Z_3\sqrt{(1-\gamma_C)\kappa_C}\left(1+Z_3^2\beta_1\sqrt{(1-\gamma_C)(1-\kappa_C)}\right)}{1-Z_3^4\beta_1\beta_2(1-\gamma_C)(1-\kappa_C)}\right]^2 \quad (3.6)$$

$$\left|\frac{E_{R1}}{E_{in}}\right|^2 = \left[\frac{-(1-\gamma_R)\kappa_R}{1-Z_1(1-\gamma_R)(1-\kappa_R)}\right]\left[\frac{j.Z_3\sqrt{(1-\gamma_C)\kappa_C}\left(1+Z_3^2\beta_2\sqrt{(1-\gamma_C)(1-\kappa_C)}\right)}{1-Z_3^4\beta_1\beta_2(1-\gamma_C)(1-\kappa_C)}\right]^2 \quad (3.7)$$

Where E_{S1} and E_{R1} represent the sensing and reference signal respectively, $\gamma_S = \gamma_0$ and $\gamma_R = \gamma_3$ are the fractional coupler intensity loss in sensing and reference unit, $\kappa_S = \kappa_3$ and $\kappa_R = \kappa_0$ are the coupling coefficient in sensing and reference unit, $Z_1 = \exp\left(\frac{-\alpha}{8}\frac{L_1}{2} - jk_n\frac{L_1}{2}\right)$, $Z_2 = \exp\left(\frac{-\alpha}{8}\frac{L_2}{2} - jk_n\frac{L_2}{2}\right)$ and $Z_3 = \exp\left(\frac{-\alpha}{8}\frac{L_3}{4} - jk_n\frac{L_3}{4}\right)$ are loss coefficients, and β is a complex coefficient, which they are described by

$$\beta_1 = \left[\frac{\sqrt{(1-\gamma_3)(1-\kappa_3)} + (1-\gamma_3).e^{\frac{-\alpha L_1}{4} - jk_n L_1}}{1-\sqrt{(1-\gamma_3)(1-\kappa_3)}.e^{\frac{-\alpha L_1}{4} - jk_n L_1}}\right] \quad (3.8)$$

$$\beta_2 = \left[\frac{\sqrt{(1-\gamma_0)(1-\kappa_0)} + (1-\gamma_0).e^{\frac{-\alpha L_2}{4} - jk_n L_2}}{1-\sqrt{(1-\gamma_0)(1-\kappa_0)}.e^{\frac{-\alpha L_2}{4} - jk_n L_2}}\right] \quad (3.9)$$

The power output P at all ports is expressed by

$$P = |E|^2 \quad (3.10)$$

For common sensing applications such as bio/chemical sensing, the interaction between molecules and sensing layer leads to change in refractive index in the layer. Consequently, the light mode supported by the ring resonator experiences this change through its evanescent field, leading to change in effective index [44]. This, in turn, results in shift in resonance wavelength of the mode. Employing Eqs. (3.11), in general, the shift in resonant wavelength with effective index and physical dimension change is given by:

$$\frac{\Delta\lambda}{\lambda} = \frac{\Delta n}{n} + \frac{\Delta L}{L} \tag{3.11}$$

The first contribution for the shift in resonance is the change in n which actually changes when the refractive index on the surface of the ring is modified by the interaction of analytes with sensing layer. Any mechanical effect leading to the change in the size of the ring structure could also modify the optical mode in the resonator and hence leading to a shift in the resonance wavelength. However, first contribution does not apply to our structure, thus the first term on the right side of the above equation can be ignored.

3.3 Sensor based on a PANDA Ring Resonator

In simulation, the sensing ring circumference L_2 is varied, in which the optical path length is also changed, and an interferometer system is formed [43, 48]. In practical if the sensing unit is coupling with other surrounding things such as DNA or molecule, so the external force was applied to the sensing unit, then the sensing unit will be deform, say in ellipse or oval shape, and then it is also cause the changed in circumference, which the ellipse circumference can be explained by Eq. (3.12).

$$L_{ellipse} = \frac{\pi}{2}\left[3(a+b) - \sqrt{(3a+b)(a+3b)}\right] \tag{3.12}$$

Where a and b are semi-major and semi-minor axis respectively.

To compare the reference and sensing signals, we set $\gamma_0 = \gamma_3$, $\kappa_0 = \kappa_3$ so $\beta_1 = \beta_2$ and then set $\gamma_S = \gamma_R$, where finally E_{S1} and E_{R1} are both identical, if $L_1 = L_2$. Then E_{S1} is varied while L_2 is changed by mean of varying R_2 with respect to E_{R1}, in which R_2 remains constant. The change in optical path length between sensing and reference signals are compared by the use of MATLAB programming, in which the induced change by the external

parameters is measured. To confirm the results the finite difference time domain method (FDTD), is also used to analyze the signal via the computer programming called Opti-wave, whereas all the parameters are simulated based on the practical parameters. The simulation steps are 40,000 iterations and the peak spectrum at reference point and sensing point are shown Fig.3. 2.

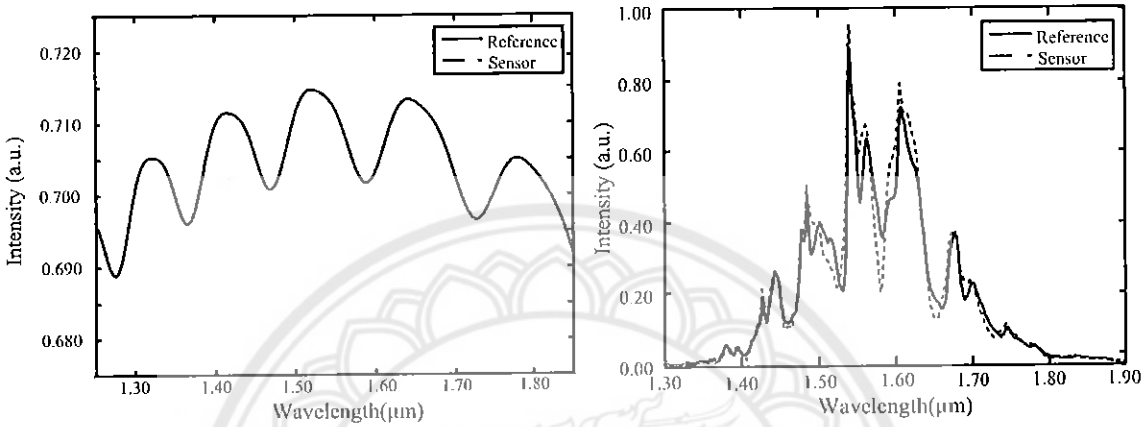

Fig.3.2. Shows the relationship between intensity and wavelength of sensing (E_{S1}), dot red line, and reference signals (E_{R1}), solid blue line, with $\Delta L = 0$, obtained by (a) MATLAB and (b) Opti-wave programming.

This measurement is formed by the comparison of the shift in wavelength (optical path length), which is called ***self-calibration***, and the difference between center peak wavelengths ($\Delta\lambda$) is obtained by

$$\Delta\lambda = \lambda_2 - \lambda_1 \tag{3.13}$$

where λ_1 and λ_2 are the peak wavelengths of Ref.1 and Sen.1, respectively. The relationships between intensity and wavelength-shift are plots as shown in Fig.3.3 by MATLAB programming and Fig.3.4 by Opti-wave computer program , which is set as a self-calibration sensing transducer.

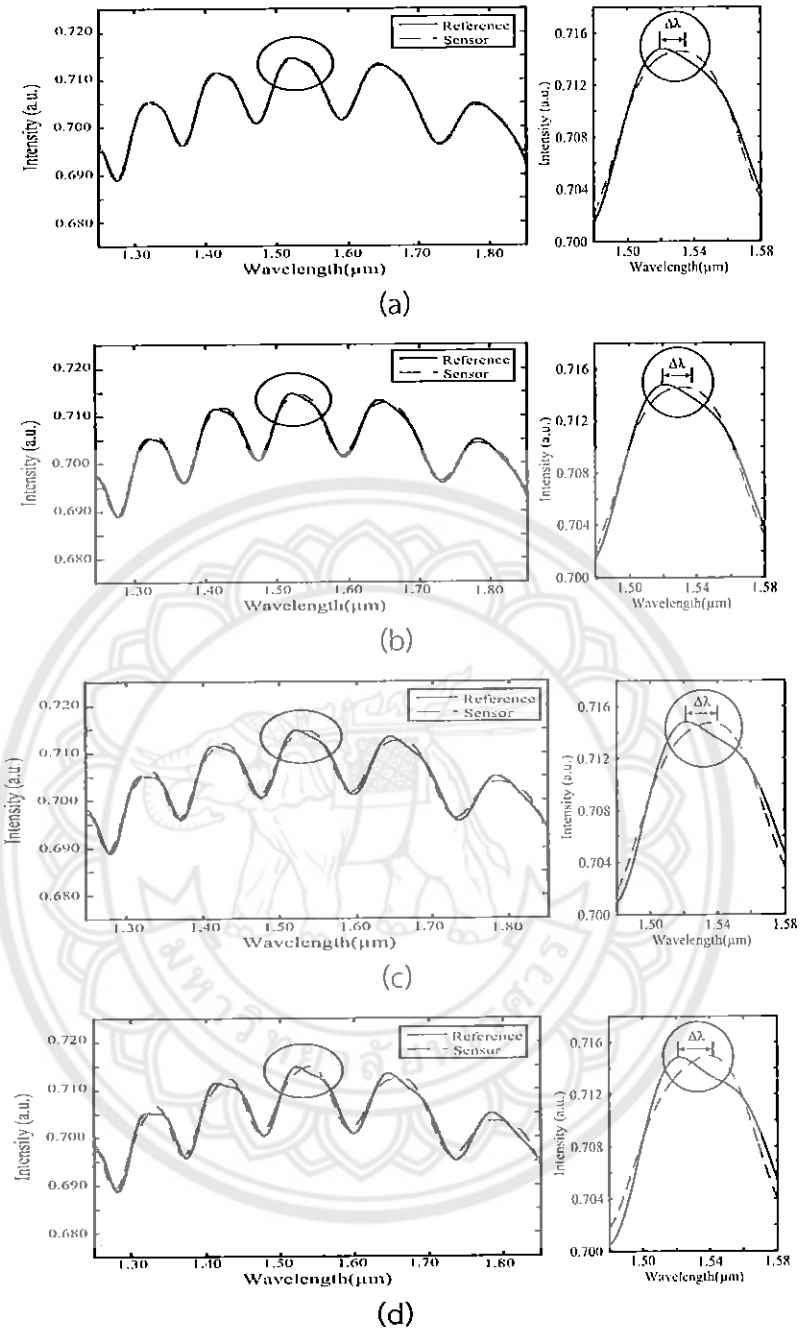

Fig.3.3. Shows the relationship between intensity and wavelength of sensing (E_{S1}), dot red line, and reference signals (E_{R1}), solid blue line, with the Ring Circumstance-shift, (a) ΔL = 0.01257 μm, (b) ΔL = 0.02514 μm, (c) ΔL = 0.03771 μm, and (d) ΔL = 0.05028 μm.

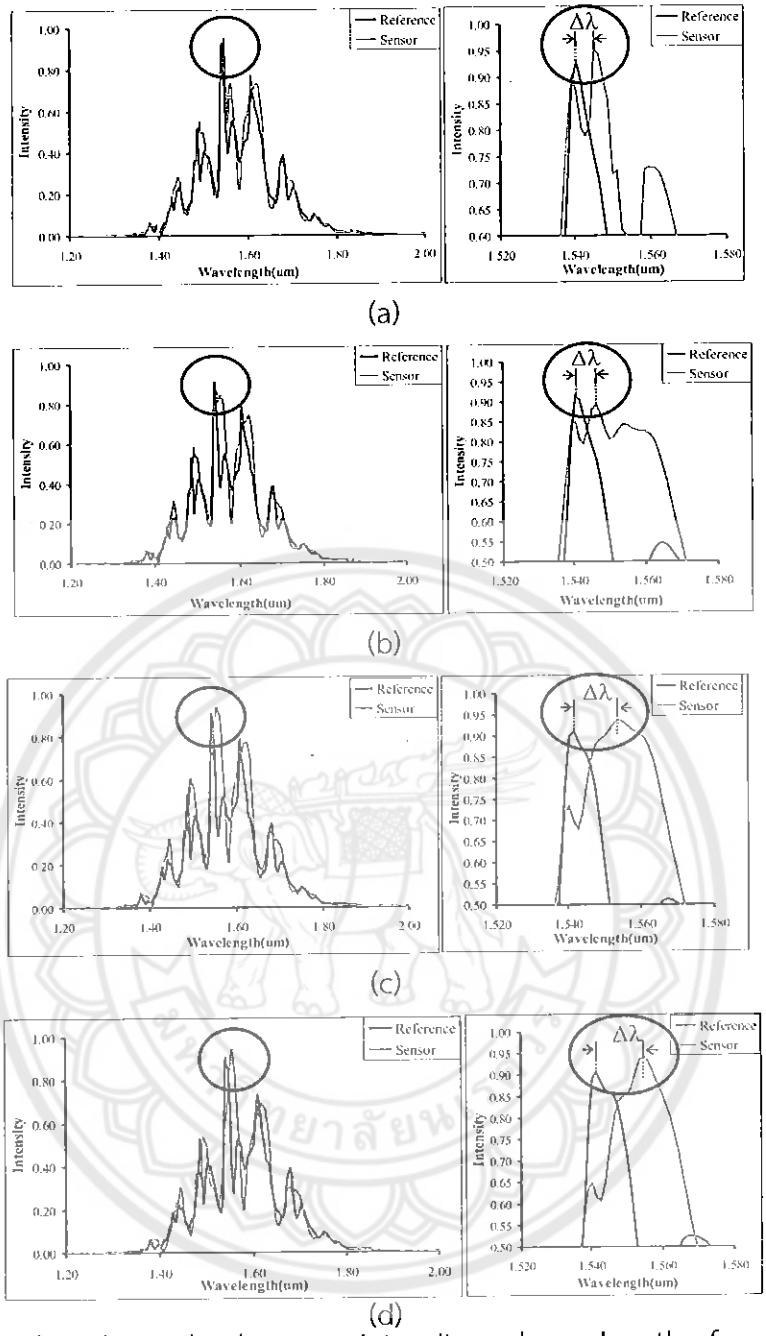

Fig.3.3. Shows the relationship between intensity and wavelength of sensing (E_{SI}) and reference signals (E_{RI}), with the Ring Circumstance-shift, (a) ΔL = 0.01257 μm, (b) ΔL = 0.02514 μm,
(c) ΔL = 0.03771 μm, and (d) ΔL = 0.05028 μm.

Both signals, i,e, sensing and reference signals are observed and compared, and the self-calibration transducer is performed [40, 41]. We assume that the load cell or others sensing parameters is applied on the second ring R_2, whereas stress and strain are introduced on the sensing unit by mean of the elastic modulus of the materials. This is caused the difference in peak spectrum of both signals, which is described by the Eqs. (3.14).

$$Y_0 = \frac{F/A}{\Delta L/L} = \frac{Stress}{Strain} \qquad (3.14)$$

and the relationship between force and the difference length is described by

$$F = \left(\frac{Y_0 A_0}{L_0}\right).\Delta L \qquad (3.15)$$

Where F is the applied force, Y_0 is the Young Modulus, A_0 is the initial cross-section area, L_0 is the initial length and ΔL is the difference in length. According to the properties of InGaAsP/InP material [45-47]

By using Eq. (3.6-3.15) the relationship between intensity and wavelength of the sensing signals, which calculated and simulated by MATLAB and Opti-wave programming respectively are show in Figs.3.3-3.4 and the results showed that they are corresponding in the same analogous. And the relationship between the ring circumstance-shift ΔL and wavelength shift, for both MATAB and Opti-wave programming are plotted as shown in Fig. 3.5, the linearity relationship between the ΔL and wavelength shift with R^2 = 0.653 is formed, which is shown in good linearity for sensing application. We found that a sensing range in terms of wavelength-shift ($\Delta\lambda$) within the resolution of 1 nm is achieved. By using the least square curve fitting, the linearity relationship between the applied force and ΔL with R2 = 1.00 is formed, which is shown in the Fig. 3.6. In this case study, the applied micro/nano force ranges were given between 0.00 and 8.00 nN.

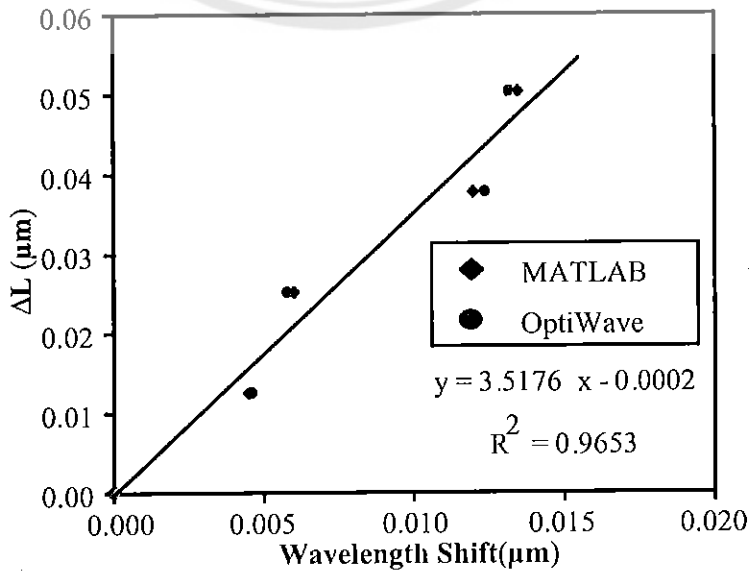

Fig.3.5. Graph of the linear relationship between Ring Circumstance-shift (ΔL) and the Wavelength-shift ($\Delta\lambda$).

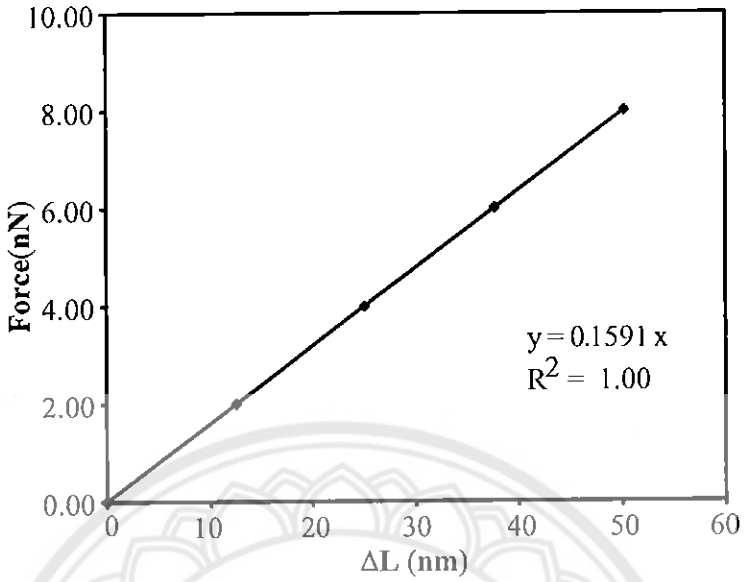

Fig.3.6 Graph of the linear relationship between Force and the ΔL.

The system have the measuring regions with in the range of 1 nm, in which the self-calibration of the measurement of two sensing and reference signal can be compared without any additional optical part or other addition unit. The calibration is allowed by using the change in wavelength between sensing and reference signals, which is existed within the system. The other advantage is that available foe network sensing applications due to the use of the integrated optic device, which has shown in the next chapter.

CHAPTER 4

BRAIN SIGNAL MONITORING MODEL

4.1 THz WGM signals

A PANDA ring circuit was modified as micro-conjugate mirror device system as show in Fig. 4.1, where the micro-optical device system can form the 3D pixel which is seen in the form of THz whispering gallery modes (WGM). The important device that can be used to construct the 3D images are the object and reference beams can be formed by the reflected light beams from the PANDA ring through and drop ports. The interference between these two beams forms the 3D pixel by the four-wave mixing behavior coupled by the two nonlinear side rings. It can be described by time-dependent Maxwell's equations and given by reference [24], where more details and references can be found in references.

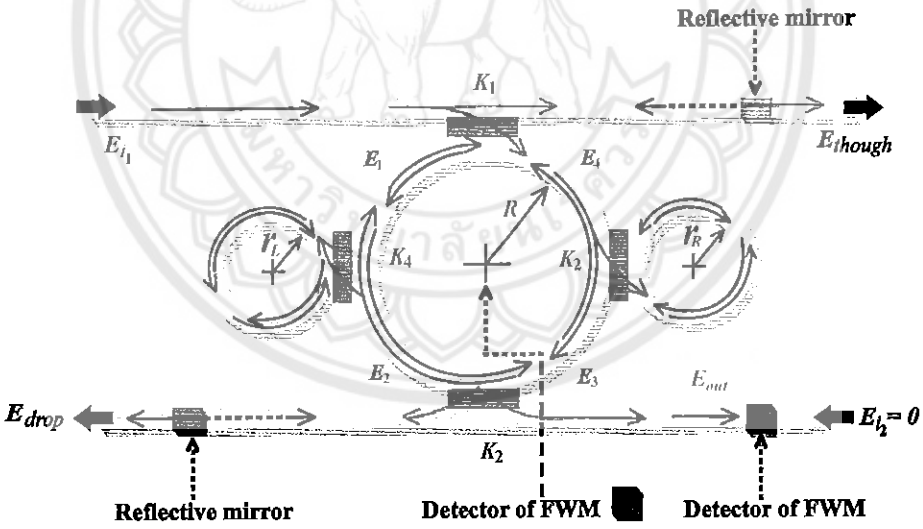

Fig. 4.1. A schematic structure of PANDA ring conjugate mirror

In simulation, THz whispering gallery modes are obtained by using the Opti-wave program with finite-difference time-domain (FDTD). The parameters of the PANDA ring resonator are fixed to be the Gaussian beams wavelength of 3.0 μm and power of 10 mN are introduced into the input port of the PANDA ring circuit. The waveguide core n=3.14, n_2 = 1.3 x 10-13 cm2/W, core area of the waveguides is A_{eff} = 0.3 μm2 and waveguide loss coefficient is α =0.1 dB/mm. The parameters for add-drop optical multiplexer and both

micro-rings on the left and right hand sides of the PANDA ring are set at $R_L = R_R = 0.775$ μm and radius of the center ring is Rad = 1.565 μm. The coupling coefficient ratios are $\kappa_0 = \kappa_3 = 0.5$, $\kappa_1 = \kappa_2 = 0.5$ μm.

The 3D pixel is seen in the form of THz whispering gallery modes at the PANDA ring center, which is the real image as show in Fig. 4.2. In addition, the conjugated mirror position was varied to obtain the appropriate positions for good 3D image quality as show in Fig. 4.3. In Fig. 4.3 shows result of the mirror manipulation in the appropriate position, which shows in the form of graphs that are characteristic of four-wave mixing with base on almost balanced or symmetric side band frequency, which is a frequency ranges from 175 - 215 THz. The balance (Δf) of upper side band (Δf_R) and lower band (Δf_L) frequencies are obtained. The nice display of the reflector within a propose device, in which the center signal will display the real time 3D images, which is the same as the Add port output signals.

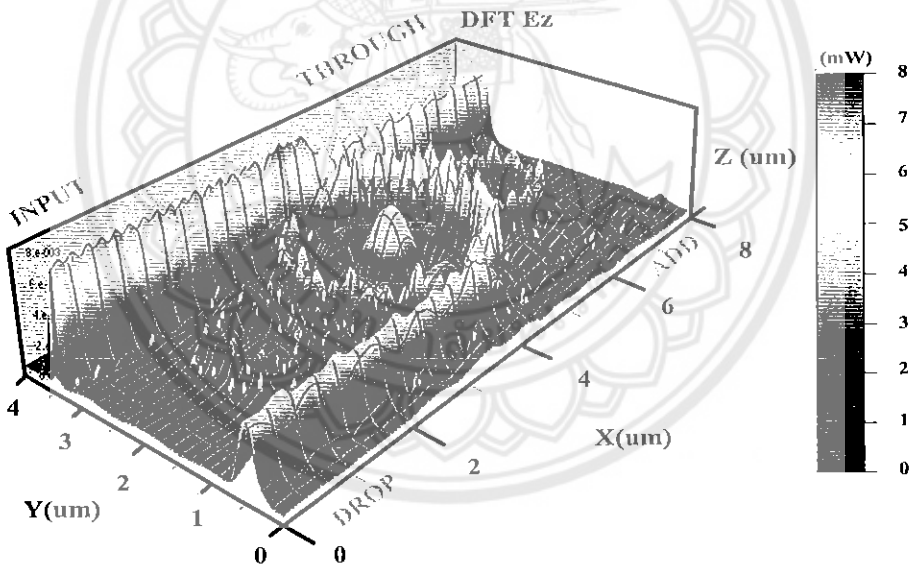

Fig. 4.2. THz whispering gallery modes (WGM) at the PANDA ring center

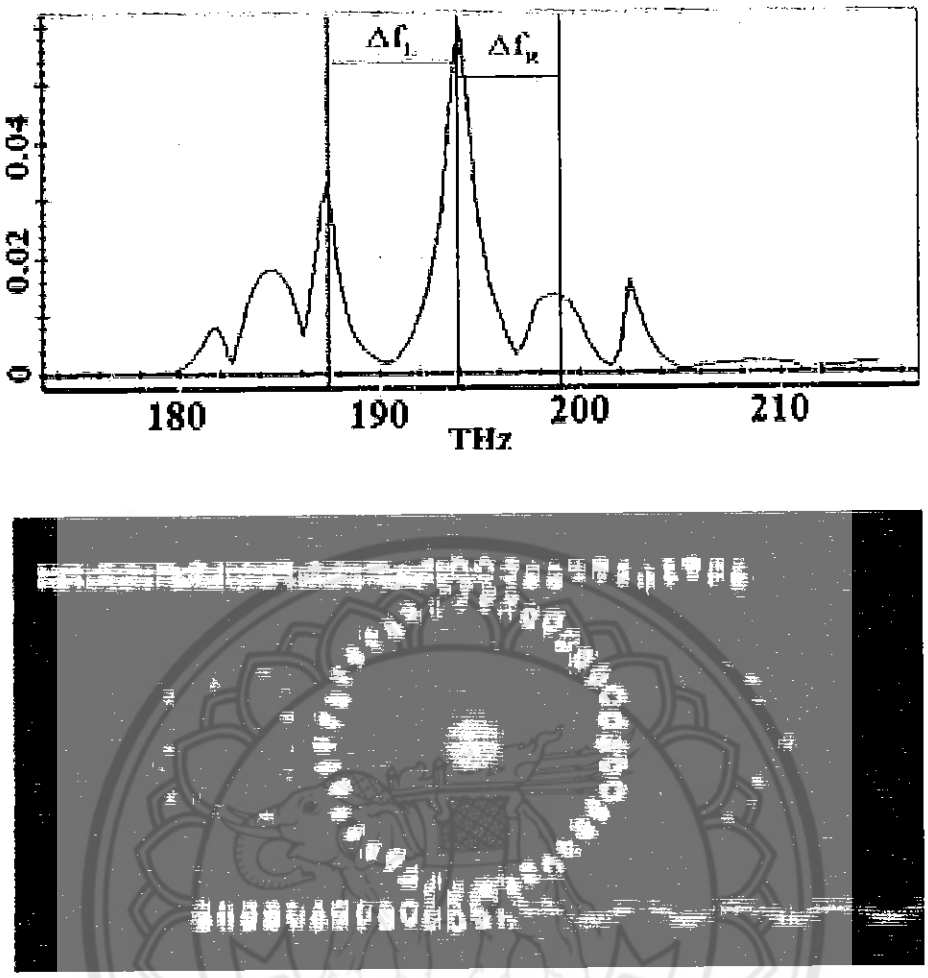

Fig. 4.3. The results of PANDA ring conjugate mirror in the symmetry FWM

4.2 Conjugate Mirror Model

A PANDA ring conjugate mirror is as shown in Fig 4.4 and 4.5 Device system can be formed the 3D pixel which is seen in the form of whispering gallery modes (WGMs). It can be described by time-dependent Maxwell's equations and given by reference, where more details and references can be found in references. Simulated experiment and result of the whispering gallery mode are obtained by using the Opti-wave program with finite-difference time-domain (FDTD). The ring material is InGaAsP/InP, where the device parameters are given in the Fig caption, which is the micrometer scale. Here, the waveguide core n=3.14 is bordered on each side by air n=1. The parameters for add-drop optical multiplexer and both microrings on the left and right hand sides of the PANDA ring are set at R_l=R_r= 0.775 μm and radius of the center ring is R_{ad}= 1.565 μm. The coupling coefficient ratios are κ_1=κ_4=0.5,

K_2=K_3=0.5, effective core area of the waveguides is A_{eff} = 0.3 μm^2, and waveguide loss coefficient is α =0.1 dB/mm.

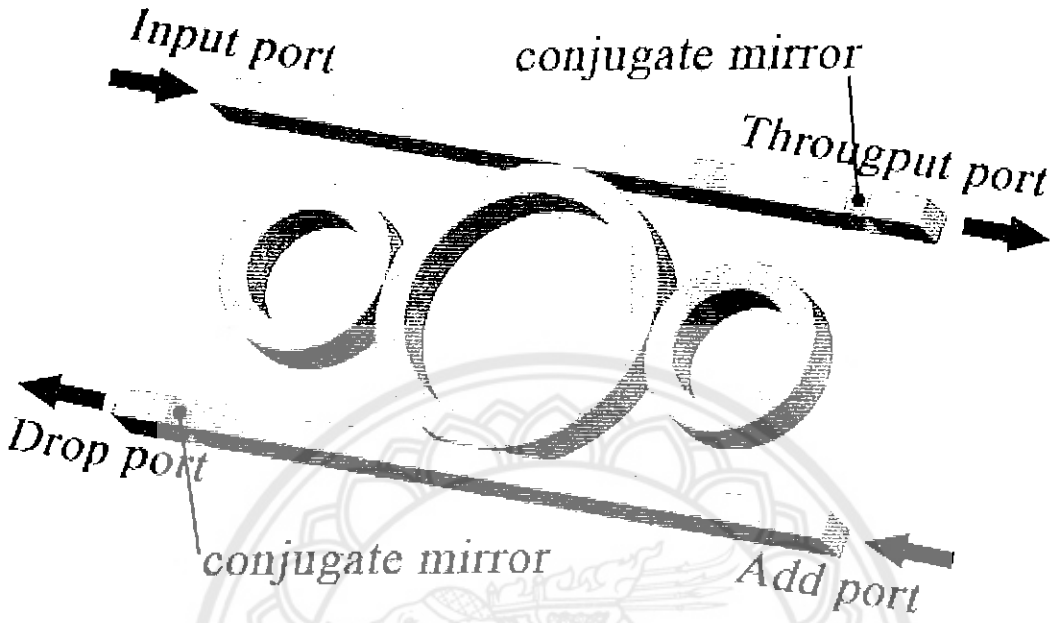

Fig 4.4. A schematic structure of PANDA ring conjugate mirror

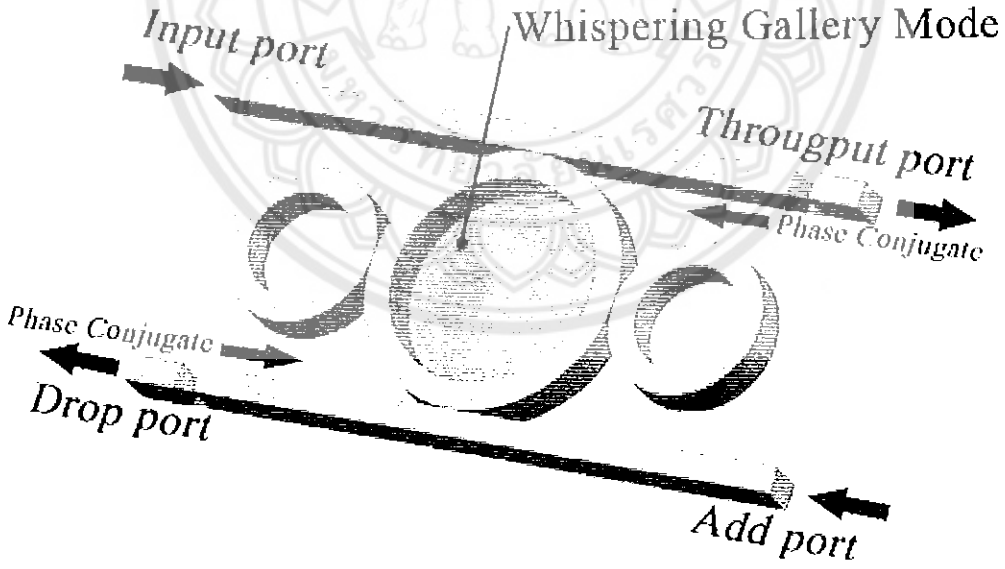

Fig 4.5. Shows the whispering gallery mode output with 3D pixel(image)

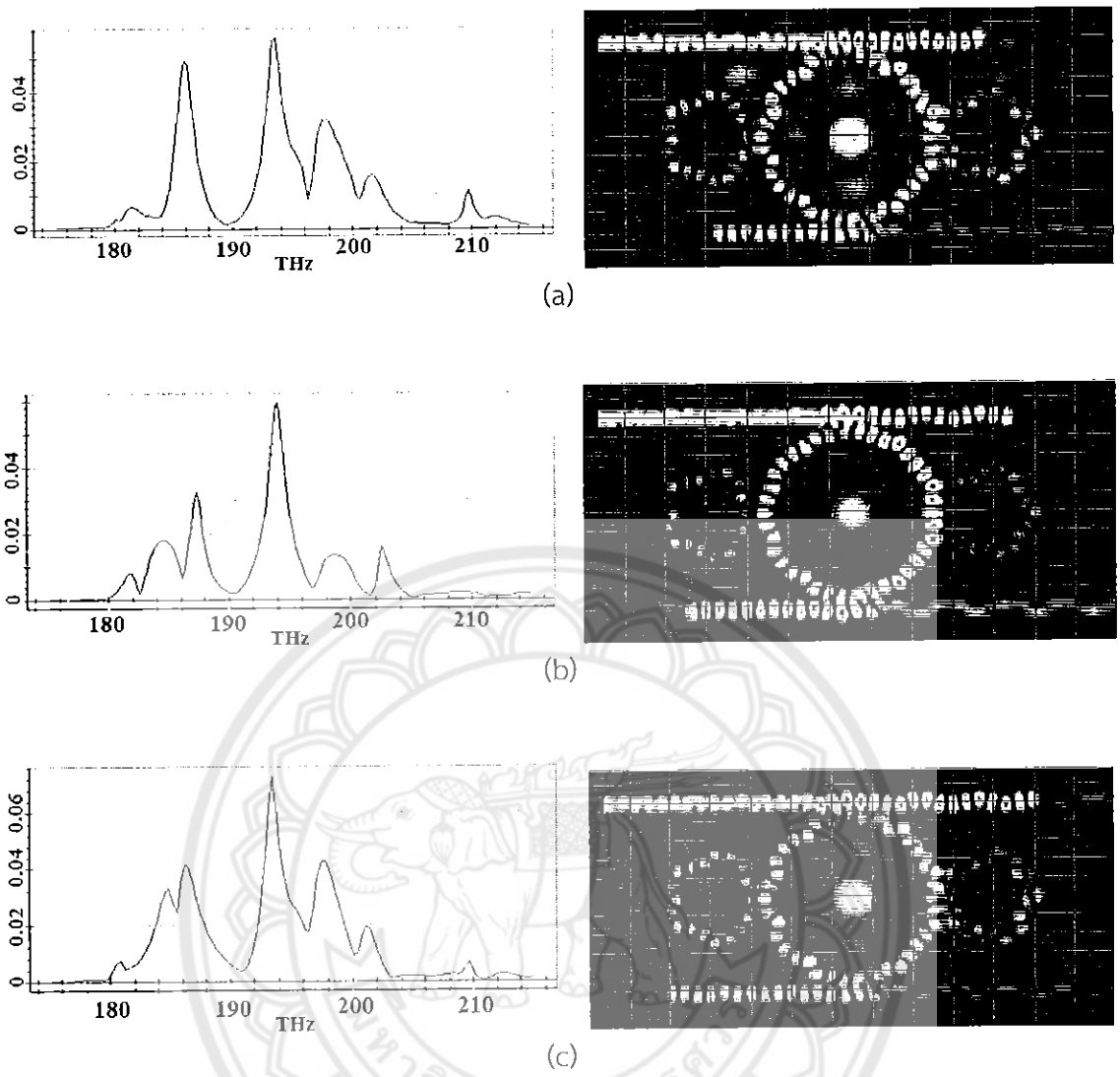

Fig 4.6. Result of PANDA ring conjugate mirror (a) distance conjugate mirror as 2.5 μm (b) distance conjugate mirror as 3 μm (c) distance conjugate mirror as 3.5 μm

In principle, the four-wave mixing behavior coupled by the two nonlinear side rings. The 3D pixel is seen in the form of whispering gallery modes at the PANDA ring center. It is real 3D pixel. The parameters of device are adjusted for simulation as refractive index of conjugate mirror and result is obtained slightly different by definition range n=1 to n= 3 without development. Then improvement parameters are changed as distance of conjugate mirror and are shown in Fig 4.6, by fixation n=1. Simulation shows 3D pixel generated and distorted images. In Fig 4.6(a) and Fig 4.6(c) shows the four-wave mixing with asymmetry. The images appear distorted result. Then Fig 4.6(b) demonstrates the four-wave mixing as symmetry and display perfect 3D pixel images.

4.3. Brain Signal Monitoring Model

In Fig. 4.7 shows the area of interaction between the electromagnetic field caused by the coupling within the PANDA ring resonator circuit and that occur within the brain when a human body is performed in response to stimuli, either within the body or outside the body, where these activities are executed in electrical form via the nerve cells to stimulate or to commit out the order in accordance with the desire. Hence, images of the brain in three dimension patterns generated by the micro-conjugate mirror appears to be the difference of pattern features based on the results obtained from the interaction of electromagnetic fields. The result of THz whispering gallery modes signal, which is the coupling effects can be measured by the output probe at the Add port (terminal output port) of the PANDA ring, where the use of probe array with also be available for a large area, i.e., distributed sensing applications as show in Fig. 4.8.

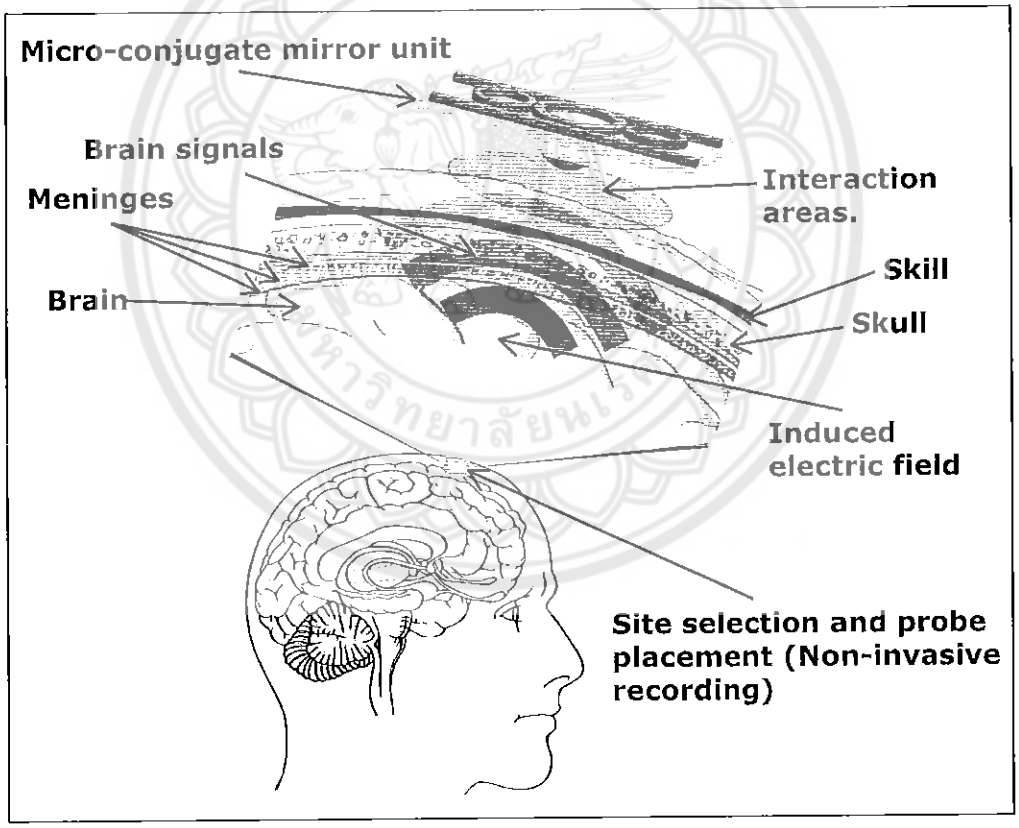

Fig. 4.7. Schematic of connection and interaction area between 3D imaging probe and brain cell (signals)

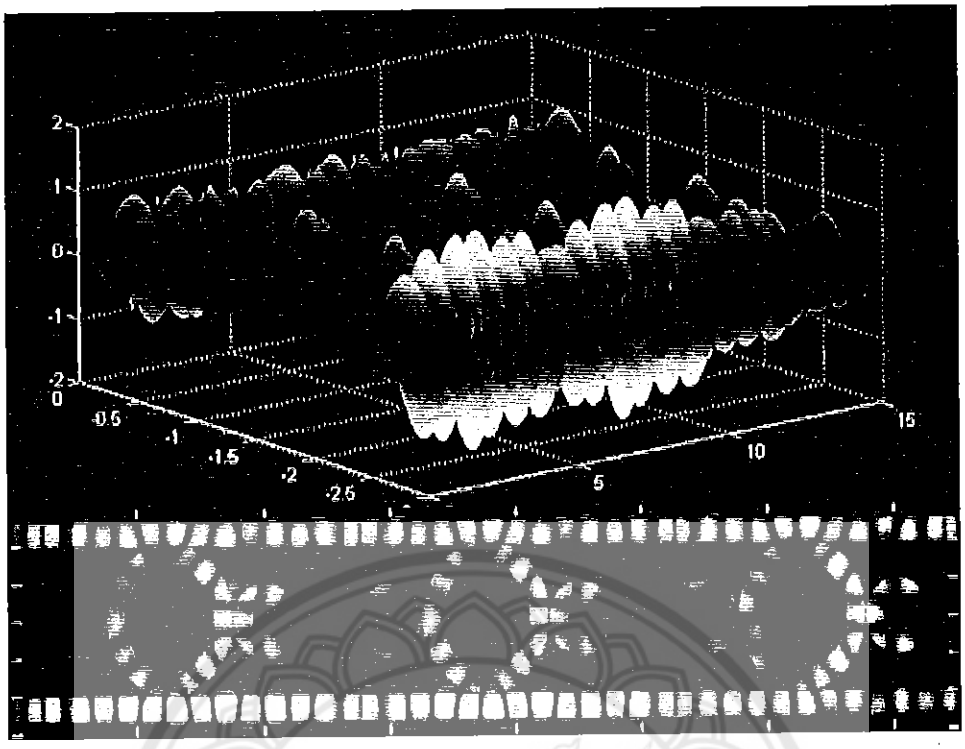

Fig. 4.8. Result of 3D image generated by a micro-conjugate mirror array (3 units or pixels)

The proposed system of application is as shown in Fig. 4.9, which consists of four main parts, where they are (i) sensing device site selection and placement, (ii) 3D image signal acquisition, (iii) signal processing and 3D image pattern recognition, and (iv) application interface. In operation, the optical sensing devices are placed by the thin film optical probe, which can penetrate to penetrate the skin, muscle, and skull into the brain without jeopardizing the brain tissue or other organs. The brain signals (coherent lights) are commonly constructed of the though, calculation, happiness, sadness, suffering, which cannot not be visible in the normal appearance. Propagation of the 3D light probe (electromagnetic field) is continuously emitted and affects the signal occurring within optical devices, which can be obtained by measuring output. Basically, when the brain signals are in normal state, the measured value of the signals can be neglected, which they are considered as the offset value. In this case, the sensor system is implemented as the transmitter of the 3D light probe, where the exchange or communicate among brain cells can be determined in terms of electrical signals, whereas the signal received from the sensor system can be a form of signals that are not appropriated for the applications. Thus, the received signals are required to be processed based on the signal processing in order to obtain the suitable brain signals, which comprises the sub-steps including (i) preprocessing to

verify the integrity of the signal, (ii) feature extraction to obtain a qualified pattern according to the process of classification. Additionally, (iii) classification (specific model) of the signal is also required, which will lead to the final step is application interface is to take a signal has applications in various fields.

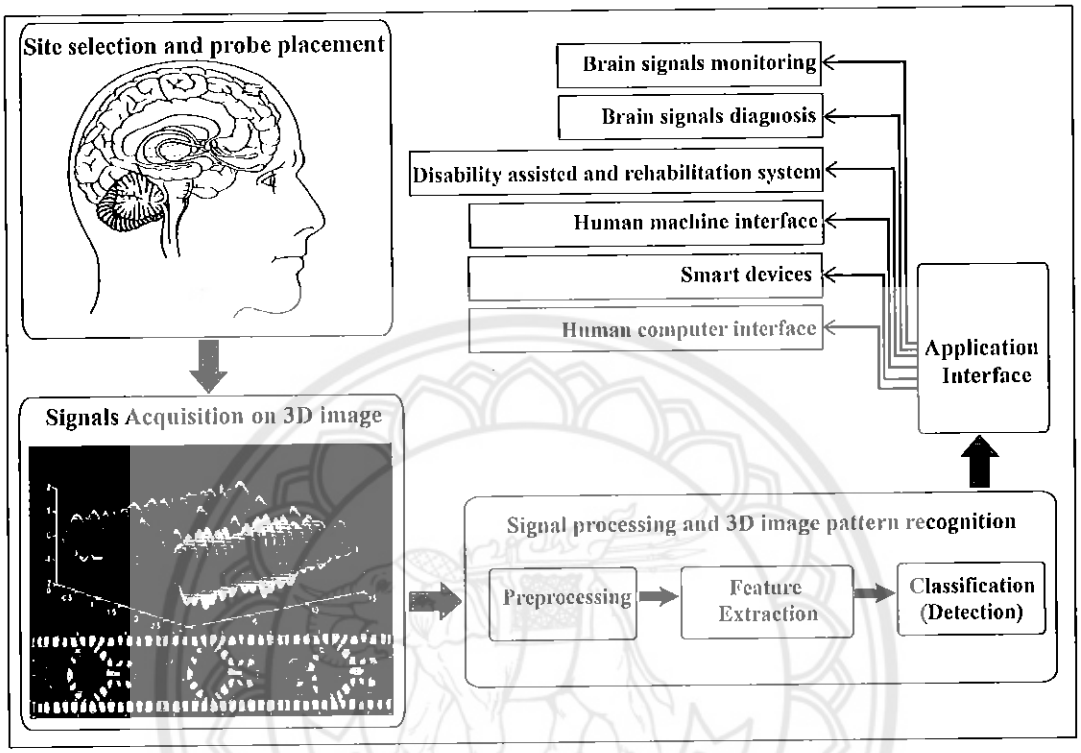

Fig. 4.9. A schematic diagram of brain signal and WGMs interconnection

CHAPTER 5

CONCLUSION

A new model of 3D pixel images using a micro-optical device system is proposed. The four-wave mixing of wave is the key functioned of such a device concept, which is based on 3D pixel image generation. The 3D images are perfectly adjusted by the four-wave mixing results. In application, the large areas(many pixels) can be constructed by the same principle, which is useful for new 3D image technology applications. Then we have demonstrated the new system of 3D brain signal monitoring and processing using micro-optical conjugate mirror based on whispering gallery modes of light within a PANDA ring circuit. Brain signals are presented in order to be used as a decision support analysis of brain abnormalities using 3D image signal information, which is formed by the THz probe signals. The THz frequency regime can be generated and formed by the micro-conjugate mirror device, which can be used to perform the brain signal connection for 3D imaging brain signal processing and interpretation. These probes (signals) can penetrate and connect to the brain cells (signals). The results can be used to form the 3D image pattern recognition study and development for the human machine interface, human computer interface, which is very useful for medical applications.

References

[1]. X. Pei, J. Hill and G. Schalk, "Silent Communication: Toward Using Brain Signals", IEEE Pulse, vol. 3, no. 1, 2012, pp.43–46.

[2]. X.-Y. WANG, J. JIN, Y. ZHANG and B. WANG, "Brain Control: Human-computer Integration Control Based on Brain computer Interface Approach", Acta Automatica Sinica, vol. 39, no. 3, 2013, pp. 208–221.

[3]. F. Zeshan and R. Mohamad, "Medical Ontology in the Dynamic Healthcare Environment", Procedia Computer Science, vol. 10, 2012, pp. 340–348.

[4]. L. Maier-Hein, P. Mountney, A. Bartoli, H. Elhawary, D. Elson, A. Groch, A. Kolb, M. Rodrigues, J. Sorger, S. Speidel and D. Stoyanov, "Optical techniques for 3D surface reconstruction in computer-assisted laparoscopic surgery", Medical Image Analysis, vol.17, no. 8, 2013, pp. 974–996.

[5]. G. Seçkin, "Cyber patients surfing the medical web: Computer mediated medical knowledge and perceived benefits", Computers in Human Behavior, vol. 26, no. 6, 2010, pp. 1694–1700.

[6]. W. Ng, D. R. Golish, H. Xin and M. E. Gehm, "3D rapid prototyping of terahertz computer-generated volume holograms", in 2012 37th International Conference on Infrared, Millimeter, and Terahertz Waves (IRMMW-THz), 2012, pp. 1–2.

[7]. N. Rothbart, H. Richter, M. Wienold, L. Schrottke, H. T. Grahn and H.W. Hubers, "Fast 2-D and 3-D Terahertz Imaging With a Quantum-Cascade Laser and a Scanning Mirror", IEEE Transactions on Terahertz Science and Technology, vol. 3, no. 5, 2013, pp. 617–624.

[8]. B. C. Q. Truong, H. D. Tuan, H. H. Kha and H. T. Nguyen, "Debye Parameter Extraction for Characterizing Interaction of Terahertz Radiation with Human Skin Tissue", IEEE Transactions on Biomedical Engineering, vol. 60, no. 6, 2013, pp. 1528–1537,

[9]. E. P. J. Parrott, Y. Sun and E. Pickwell-MacPherson, "Terahertz spectroscopy: Its future role in medical diagnoses", Journal of Molecular Structure, vol. 1006, no. 1–3, 2011, pp. 66–76.

[10]. K.-W. Kim, H. Kim, J. Park, J. K. Han and J.-H. Son, "Terahertz Tomographic Imaging of Transdermal Drug Delivery", IEEE Transactions on Terahertz Science and Technology, vol. 2, no. 1, 2012,pp. 99–106.

[11]. P. Bakopoulos, I. Karanasiou, N. Pleros, P. Zakynthinos, N. Uzunoglu and H. Avramopoulos, "A tunable continuous wave (CW) and short-pulse optical source for THz brain imaging applications", Meas. Sci. Technol., vol. 20, no. 10, 2009,pp. 104001.

[12]. B. St.Peter, S. Yngvesson, P. Siqueira, P. Kelly, A. Khan, S. Glick and A. Karellas, "Development and Testing of a Single Frequency Terahertz Imaging System for Breast Cancer Detection", IEEE Journal of Biomedical and Health Informatics, vol. 17, no. 4, 2013, pp. 785–797.

[13]. W. E. Baughman, H. Yokus, S. Balci, D. S. Wilbert, P. Kung and S. M. Kim, "Observation of Hydrofluoric Acid Burns on Osseous Tissues by Means of Terahertz Spectroscopic Imaging", IEEE Journal of Biomedical and Health Informatics, vol. 17, no. 4, 2013, pp. 798–805.

[14]. J. Ding, M. Kahl, O. Loffeld and P. H. Bolivar, "THz 3-D Image Formation Using SAR Techniques: Simulation, Processing and Experimental Results", IEEE Transactions on Terahertz Science and Technology, vol. 3, no. 5, 2013, pp. 606–616.

[15]. H. Tavernier, P. Salzenstein, K. Volyanskiy, Y. K. Chembo and L. Larger, "Magnesium Fluoride Whispering Gallery Mode Disk-Resonators for Microwave Photonics Applications", IEEE Photonics Technology Letters, vol. 22, no. 22, 2010, pp. 1629–1631.

[16]. S. L. McCall, A. F. J. Levi, R. E. Slusher, S. J. Pearton and R. A. Logan, "Whispering-gallery mode microdisk lasers", Applied Physics Letters, vol. 60, no. 3, 1992, pp. 289–291.

[17]. A. Taeb, S. Gigoyan, G. Rafi, S. Safavi-Naeini and M. Neshat, "A low cost and sensitive sensor based on the Whispering Gallery Mode at D-band", in Microwave Conference (EuMC), 2011 41st European, 2011, pp. 619–622.

[18]. R. Siriroj, N. Thammawongsa and P. P. Yupapin, "Micro Energy Source Using WGMs of Wave in Small Scale Optical Device", Energy Procedia, vol. 34, 2013, pp. 1–8.

[19]. K. Srinuanjan, S. Kamoldilok, W. Tipaphong and P. P. Yupapin, "A Nano-scale Transducer using a PANDA Type Ring Resonator for Gas sensor Applications", Optik - International Journal for Light and Electron Optics, (123)6, 2012, pp .475–478.

[20]. K. Tamee, K. Srinuanjan, S. Mitatha and P. P. Yupapin, "Distributed Sensors Using a PANDA Ring Resonator Type in Multiwavelength Router", IEEE Sensors Journal, vol. 11, no. 9, pp.1987–1992, 2011.

[21]. P. Sarayut, and P. P. Yupapin, "Wave-particle duality probe model using micro-optical device for neuro-quantum investigations", ScienceJet, 3: 61, 2014.

[22]. P. P. Yupapin, N. Thammawongsa and J. Ali, "Consciousness and subconsciousness detection model under Čerenkov radiation", Microwave and Optical Technology Letters, Vol. 56, Issue 7, 2014, pp. 1584–1587.

[23]. J. Rangsan and P. P. Yupapin, "Transmission characteristics of optical pulse in nested nonlinear microring resonators and gratings", JOSA B, Vol. 31, Issue 3, 2014, pp. 474-477.

[24]. K.S. Yee, Numerical solution of initial boundary value problems involving Maxwell's equations in isotropic media, IEEE Transaction on Antennas Propagation, vol.14, 1966, pp.302-307.

[25]. E. Waks and V. Jelena, Coupled mode theory for photonic crystal cavity-waveguide interaction, Optics Express, vol.13, 2005, pp.5064-5073.

[26]. N. Thammawongsa, N. Moonfangklang, S. Mitatha and P.P. Yupapin, Novel nano-antenna system design using photonics spin in a panda ring resonator, PIER L, vol.31, 2012, pp.75-87.

มหาวิทยาลัยนเรศวร